High-speed videomicroscopy and magnetorheology under triaxial unsteady magnetic fields

O. Martínez-Cano,[1,*] J. R. Morillas,[1,*,†] J. Ruiz-Nievas,[1] G. Camacho,[1]
A. Rodríguez-Barroso,[1] J. Ramírez,[2] and J. de Vicente[1]

[1]*F2N2Lab, Magnetic Soft Matter Group and Excellence Research Unit 'Modeling Nature' (MNat), Department of Applied Physics, Faculty of Sciences, University of Granada, C/Fuentenueva s/n, 18071 - Granada, Spain*

[2]*Department of Signal Theory Networking and Communications, School of Technology and Telecommunications Engineering, University of Granada, C/ Periodista Daniel Saucedo Aranda s/n, 18014 - Granada, Spain*

(Received 12 July 2024; accepted 9 December 2024; published 13 February 2025)

We describe a custom-built device that is capable of superimposing triaxial unsteady magnetic fields on a sample at the same time that its microstructure is visualized using a high-speed camera and its rheological properties are measured with a commercial rheometer. The device reaches field strengths up to 5 kA $\cdot$ m^{-1}, frequencies up to 4 kHz, and its functionality is evaluated by testing magnetorheological fluids under steady shear flow and field transients. Striking differences are found at small Mason numbers by changing the field configuration.

DOI: 10.1103/PhysRevE.111.025415

I. INTRODUCTION

Conventional magnetorheological (MR) fluids are suspensions of micron-sized magnetic particles in a nonmagnetic carrier [1–4]. By simply tuning the external magnetic field, the particles aggregate to form field-directed structures eventually having a strong impact on the rheological properties of the MR fluid. The case of uniaxial steady fields has been extensively investigated in the literature [5–8], concluding that MR fluid rheology is basically controlled by the particle concentration (ϕ) and the so-called Mason number (Mn) [9–11], i.e., the ratio between (shear flow induced) hydrodynamic and magnetic forces. For reasons that will become clear shortly, we will refer to this ratio as the flow-field-induced Mn. This designation corresponds to the classical definition in magnetorheology (see Table I) and facilitates the distinction between the traditional preyield and postyield regimes, corresponding to low and high flow-field-induced Mn, respectively.

Currently the focus seems to be on the superposition of triaxial unsteady fields [11–16]. The particle structures formed at rest (no flow) under those fields were thoroughly investigated by Martin and coworkers using experiments and simulations [12,17,18]. A particularly interesting case is that of precession fields. These fields are the superposition of a uniaxial steady field (in the following we will call them uniaxial DC fields) and a perpendicular rotating field. At low field frequencies, particle chains can move in synchronization with the field, generating a body torque along the sample and promoting interchain collisions and coalescence during chain motion [18]. At high frequencies, drag from the quiescent carrier fluid prevents particles from following the field's temporal variations, introducing time-averaged magnetic interactions. These interactions can differ significantly from those occurring under a DC field. For example, a balanced triaxial field suppresses dipolar interactions by compensating for time-averaged effects, generating a centrosymmetric magnetic force due to the external magnetic field. In this scenario, the magnetization of neighboring particles creates a local magnetic field that leads to many-body interactions, and the formation of exotic static structures that are not possible under pair-potential interactions (such as gel-like percolating networks or cellular structures) [17].

The change in the nature of the induced structures, from dynamic to static, depends not only on the field frequency but also on the ratio between the hydrodynamic forces (which arise from the dynamic motion of the structures as they follow the unsteady magnetic field) and the magnetic forces. In the literature, this ratio is referred to as the Mason number as well [10,11]. Therefore, to distinguish the different origins of the hydrodynamic forces, we will refer to this second Mn as the magnetic-field-induced Mn. Table I summarizes the expressions of Mn for each magnetic field configuration used in this study. It is important to note that under classical uniaxial DC magnetic fields, the structures are always quasistatic, so there is no need to define a magnetic-field-induced Mn for this case.

In addition to precession fields, there is a wide variety of magnetic field configurations that allow for fine-tuning of the internal microstructure of the sample and ultimately its macroscopic properties, such as conductivity or permeability [12]. However, up to date there seems to be only a few publications on the rheological properties of MR fluids subjected to triaxial unsteady magnetic fields [11,13,15,16].

*These authors contributed equally to this work
†Contact author: jmorillas@ugr.es

TABLE I. Mason number definitions. η is the carrier fluid viscosity. $\dot{\gamma}$ is the shear rate. f is the frequency of the field. θ_p is the precession and maximum angle for precession and perturbation fields, respectively. μ_0 is the permeability of vacuum. $\beta = (\mu_{pr} - \mu_{cr})/(\mu_{pr} + 2\mu_{cr})$ is the contrast factor with μ_{cr} (μ_{pr}) the relative magnetic permeability of the carrier fluid (particles). H is the external magnetic field strength.

Flow-field-induced Mason number		
Steady shear rate	$\frac{8\eta\dot{\gamma}}{\mu_0\mu_{cr}\beta^2H^2}$	Ref. [9]
Magnetic-field-induced Mason number		
Rotating magnetic field	$\frac{32\pi\eta f}{\mu_0\mu_{cr}\beta^2H^2}$	Ref. [10]
Perturbation triaxial magnetic field	$\frac{32\pi\eta f\theta_p}{\mu_0\mu_{cr}\beta^2H^2}$	Ref. [11]
Precession triaxial magnetic field	$\frac{32\pi\eta f\theta_p}{\mu_0\mu_{cr}\beta^2H^2}$	Ref. [16]

Donado *et al.* [11] reported an experimental investigation on the shear viscosity of MR fluids aggregated under the presence of perturbation fields. These fields were generated by superposition of a uniaxial DC field and a uniaxial oscillatory field in the orthogonal direction. MR fluids aggregated under low-frequency and low-amplitude perturbation fields exhibited a larger viscosity than under conventional uniaxial DC fields, presumably due to the formation of thicker aggregates. More recently, Terkel and coworkers [13,15,16] demonstrated that not only the steady shear response but also the rheological performance in dynamic oscillation can be enhanced using triaxial unsteady fields during the aggregation step prior to shearing the sample. Several field configurations were tested that yielded a bolstered storage modulus response as compared to the uniaxial DC case. Moreover, the gap between uniaxial DC and rotating fields was extensively explored through experiments and simulations in a wide magnetic-field-induced Mn range.

Unfortunately, the magnetic field generator used in previous publications did not allow visual access to the sample during the rheological tests [11,13,15,16]. In this work we carry out high-speed video-microscopy experiments in a flowing MR fluid subjected to triaxial unsteady magnetic fields. We design and construct a custom-built magnetorheometer and describe *in situ* video-microscopy studies of self-assembly under triaxial unsteady magnetic fields as well as structure evolution under the superposition of a shearing flow and a field configuration.

II. RESULTS AND DISCUSSION

The experimental setup (see Fig. 1) comprises a high-speed camera (Mini UX Photron) coupled to a 6.5× zoom lens, an LED ring providing darkfield illumination to have a high contrast and distinguish the particles from the carrier liquid, a homemade triaxial field generator to superimpose the (steady and unsteady) magnetic fields and a torsional rheometer (MCR501 Anton Paar) operating in parallel plate configuration to generate flow kinematics. All those elements were carefully synchronized (see the technical details in the Appendix).

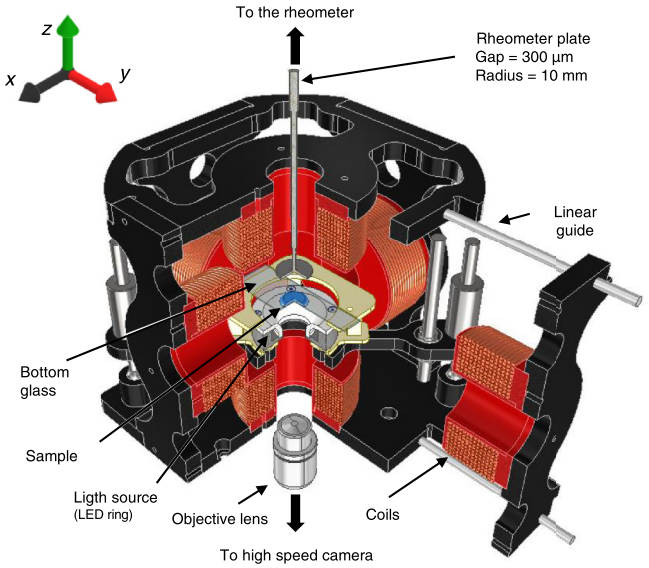

FIG. 1. Schematics of the experimental setup comprising the camera, the light source, the magnetic field generator, and the rheometer. The camera and the light source are synchronized to the rheometer to take a picture and illuminate the sample every time a rheological data is recorded. The sample is confined between the upper plate geometry of the rheometer and a bottom transparent glass. In this configuration, the images are obtained in the flow-vorticity plane (xy).

The design of the field generator bears in mind several related requisites to perform rheological experiments, visualize the sample, and apply magnetic fields concurrently. It consists of six coils, two connected in series for each orthogonal axis, centered at the faces of a cube. Its symmetry makes the magnetic field in the center (where the sample is located) have maximum homogeneity and eases aligning the generator with the rotational axis of the rheometer as well. Since the generator sits on top of the rheometer, its total volume and weight were fitted to this constraint. Coil size is chosen in order to leave enough room inside the generator and place there the sample, the illumination system, and the rheometer's plate. What is more, to have access to the inside, one of the coils is mobile along a linear guide. Finally, coils are wounded around inner holes through which measurement elements can be approached. Those holes also set the illumination path and a wide field of view to image the full radius of the sample.

Figure 2(a) shows the relationship between the current imposed on each axis and the generated magnetic field strengths, with a resulting slope of 1.6 $(\mathrm{kA}\cdot\mathrm{m}^{-1})/\mathrm{A}$. The generator maintains a constant current up to a bandwidth of 4 kHz, as shown in Fig. 2(b). Those high frequencies are obtained without a noticeable attenuation by compensating the inductive reactance of the coils with a fractal bank of selectable capacitors connected in series to each pair of coils following Ref. [19]. The result is a power circuit with a RLC configuration designed to work in resonance. Generated magnetic fields can be aligned in any 3D direction [Fig. 2(c)] while having acceptable spatial homogeneity within the sample area [Fig. 2(d)] with a relative error lower than 15% for a rheometer plate of 20 mm diameter. Field components

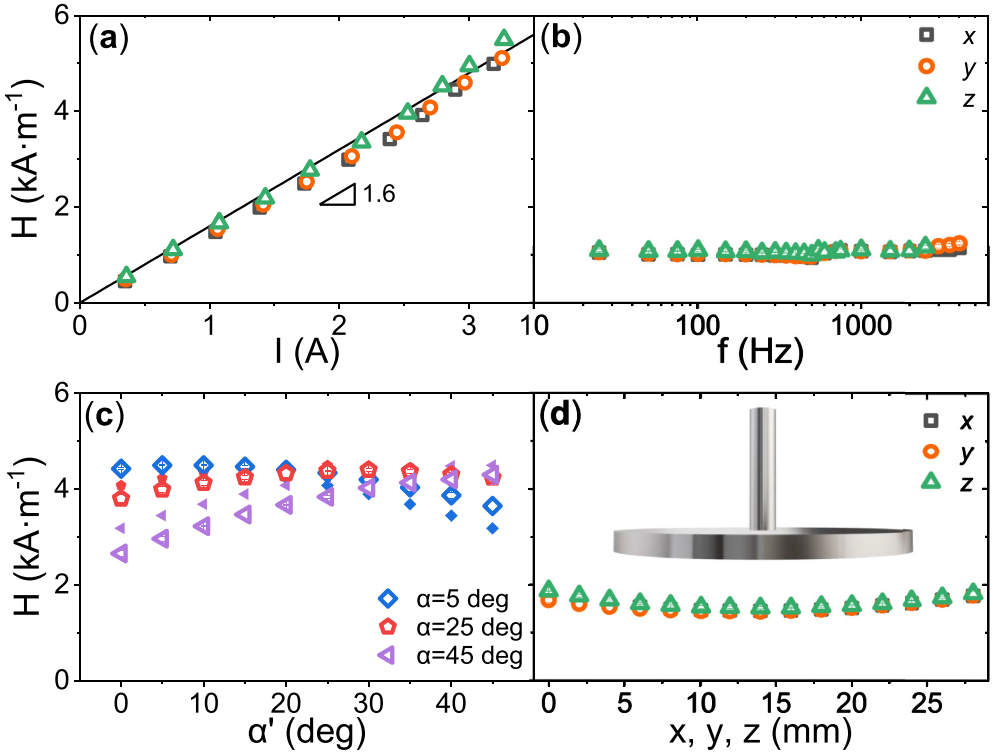

FIG. 2. Magnetic field calibration curves. (a) Relationship between applied current and measured magnetic field strength in the center of the device for each axis. (b) Frequency response in the RLC circuit for each axis at 1 A. Discrepancies at 400 Hz are due to the bandwidth of the teslameter. (c) Magnetic field strength under rotation of the teslameter probe in the flow-vorticity (xy) plane. α corresponds to the angle of the magnetic field vector and α' corresponds to the angle of the probe. It is expected that the measured magnetic field reaches a maximum when the angle of the probe matches that of the field vector. Filled symbols are the theoretical values $H(\alpha') = H_0 \cos(\alpha - \alpha')$ with $H_0 = 4.5\,\mathrm{kA\,m^{-1}}$. (d) Homogeneity of the magnetic field along each axis at 1 A. A sketch of the rheometer upper plate is also included to highlight the sample area (only for x and y axes).

can also be varied in time at different frequencies while changing the alignment yielding a wide variety of Lissajous trajectories [20,21].

Video-microscopy observations in the flow-vorticity (xy) plane of the sample are recorded placing the objective lens and camera beneath and outside the generator, with the optical axis parallel to the rotational axis of the rheometer (Fig. 1). Quality images are obtained thanks to the highly intense and homogeneous illumination provided by an LED ring on top of which the sample lies. The LED is synchronized with the rheometer and camera to work in flash mode. In this way, light and image capture are triggered only by the rheometer measurements avoiding sample overheating during long operation times. Taken images are further analyzed to get microstructural information of the sample as it self-assembles and/or evolves under shear flow. Namely, the percentage of occupation (PoO) and characteristic size (CS) of the particle aggregates are studied.

The potential of the device is demonstrated through two types of experiments in which the MR fluid is subjected to a wide range of flow- and magnetic-field-induced Mn values, allowing for the testing of the rheological properties of both static and dynamic structures in the pre- and postyield regimes. In all cases, the MR fluid concentration was $\phi = 2.5$ vol%, and external field strength was $H = 4\,\mathrm{kA\,m^{-1}}$.

In the first experiment, it is interrogated the steady rheological response of the structures induced by a precession field (rotating/DC component in the xy plane/along the z axis). To do so, the sample was self-assembled during 30 s using a precession angle of 25° and frequencies of 1, 10, or 100 Hz (magnetic-field-induced Mn of 0.06, 0.6, and 6, respectively). Next, the structure was frozen by applying a uniaxial DC field and the shear rate was varied using a logarithmic ramp up to 1000 $\mathrm{s^{-1}}$ to measure the shear stress and construct the complete flow curve (flow-field-induced Mn $\in [0.01, 10]$). For comparison, the experiment was repeated both in the absence of a magnetic field and with the application of a uniaxial DC field during the self-assembly step as well.

In the second experiment, the shear rate was fixed at a low value (3 $\mathrm{s^{-1}}$, low flow-field-induced Mn of 0.03, thus in the preyield regime) during the whole experiment and, at a given time, a magnetic field was suddenly applied to promote the field-induced self-assembly. The experiment was repeated for different field configurations (uniaxial DC, precession with angle of 25°, perturbation with maximum angle of 25° and rotating fields) and different field frequencies (1, 10, and 100 Hz). In all cases, the DC component was along the z direction (except the rotating field that was contained in the xy plane). These different configurations and frequencies result in magnetic-field-induced Mn values of 0.06, 0.6, and 6 (for precession and perturbation fields) and 0.12, 1.2, and 12 (for rotating fields). The transient response following the removal of the field was also measured; however, no hysteresis or distinctive effects were observed.

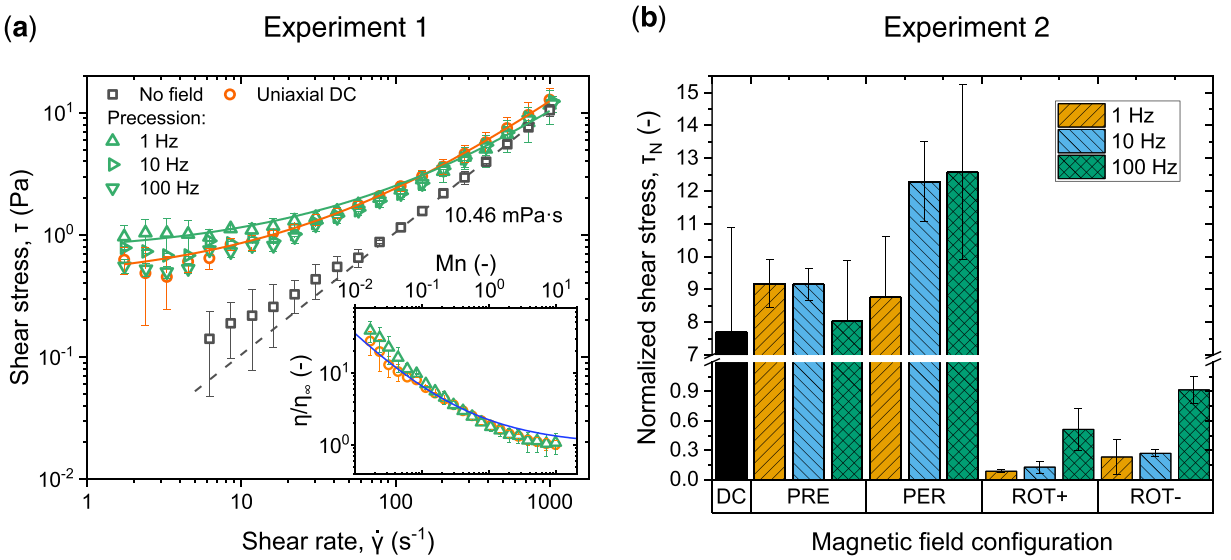

FIG. 3. Rheological behavior of a MR fluid under shear flow and triaxial magnetic fields. (a) Experiment 1: Shear stress versus shear rate curves for three different cases: no field (squares), uniaxial DC field (circles), and precession field of different frequencies (triangles). Dashed/solid lines correspond to a linear/Casson model fit. Inset: Same data plotted as dimensionless viscosity η/η_∞ versus flow-field-induced Mason number Mn (master curve). η_∞ is calculated by linear fitting of the no field data. The blue line is the theoretical prediction according to Ref. [26]. For the sake of clarity, Casson fit and dimensionless data are shown only for uniaxial DC and 1 Hz precession cases. (b) Experiment 2: Normalized shear stress obtained with different magnetic field configurations and a shear rate of $\dot{\gamma} = 3\,\mathrm{s}^{-1}$. DC: Uniaxial DC field. PRE: Precession field. PER: Perturbation field. ROT+/ROT-: Rotating field rotating in the same/opposite direction as the shear flow. The shear stress has been averaged over the last 150 s after the field application once the MR fluid is in steady state. In both experiments, particle concentration is $\phi =$ 2.5 vol%, gap is $h = 300\,\mu\mathrm{m}$, and external magnetic field strength is $H = 4\,\mathrm{kA}\cdot\mathrm{m}^{-1}$.

The results corresponding to the first experiment are gathered in Fig. 3(a). There, the steady shear stress versus shear rate curve is shown for three cases: no field, uniaxial DC field, and precession fields of different frequencies. In the absence of the magnetic field the MR fluid behaves as a Newtonian liquid with a stress that is basically proportional to the shear rate. However, for MR fluids assembled under a magnetic field (being either uniaxial DC or precession) the MR fluid features an apparent yield stress. Its value, obtained by data fitting to the Casson model [22], is shown in Table II. Interestingly, the suspension assembled under a precession field of sufficiently small frequency exhibits a significant larger yield stress than the suspension assembled under a uniaxial DC field at the shear rate $1.74 \pm 0.19\ \mathrm{s}^{-1}$ and within the range between $3.3 \pm 1.3\ \mathrm{s}^{-1}$ and $8.5 \pm 0.9\ \mathrm{s}^{-1}$ (comparisons based on t tests with a significance level of 90%).

Since the yield stress is measured under a uniaxial DC field in all cases (implying a similar type of particle interaction), the observed differences in yield stress values can be attributed to variations in the microstructures formed under different field configurations during the self-assembly step. This process is illustrated in Movie S1 (see the Supplemental Material [23]) for both uniaxial DC and 1 Hz precession fields. The low frequency of the precession field (i.e., low magnetic-field-induced Mn) allows the induced chains to dynamically follow the temporal evolution of the magnetic field. This results in a dynamic microstructure where chains continuously sweep their surroundings, colliding and merging with neighboring chains or particles. Over time, this enables the captured particles to rearrange into densely packed, defect-free configurations within the chains. In contrast, assembly under a uniaxial DC field occurs more abruptly, driving the particles into kinetically arrested states. While this also produces a collection of chains, these are looser and more open compared to those formed under the precession field.

TABLE II. Fitting parameters to the Casson model $\tau^2 = \tau_y^2 + (\eta_\infty\dot{\gamma})^2$ for uniaxial DC and precession fields (PRE, angle of 25°) of different frequencies.

	f(Hz)	τ_y(Pa)	η_∞(mPa·s)
DC		0.406 ± 0.014	8.4 ± 0.3
	1	0.704 ± 0.004	5.67 ± 0.13
PRE	10	0.504 ± 0.022	5.8 ± 0.3
	100	0.339 ± 0.013	7.7 ± 0.3

The packed or loose nature of the chains was quantitatively assessed through image analysis. Figures 4(a1) and 4(b1) present snapshots of the particle aggregates taken at the end of the self-assembly step. From these images, it was determined that for a similar percentage of occupation (PoO) of approximately 73%, the characteristic size (CS) of the aggregates is CS = 0.195 mm for the uniaxial DC field and CS = 0.100 mm for the 1 Hz precession field. Based on these results, an inverse relationship between yield stress and CS can be established. Specifically, the DC field promotes the formation of loose and open aggregates, which are likely far from equilibrium and lack strong conformation. Consequently, these aggregates are thicker (larger CS) and mechanically weaker (lower

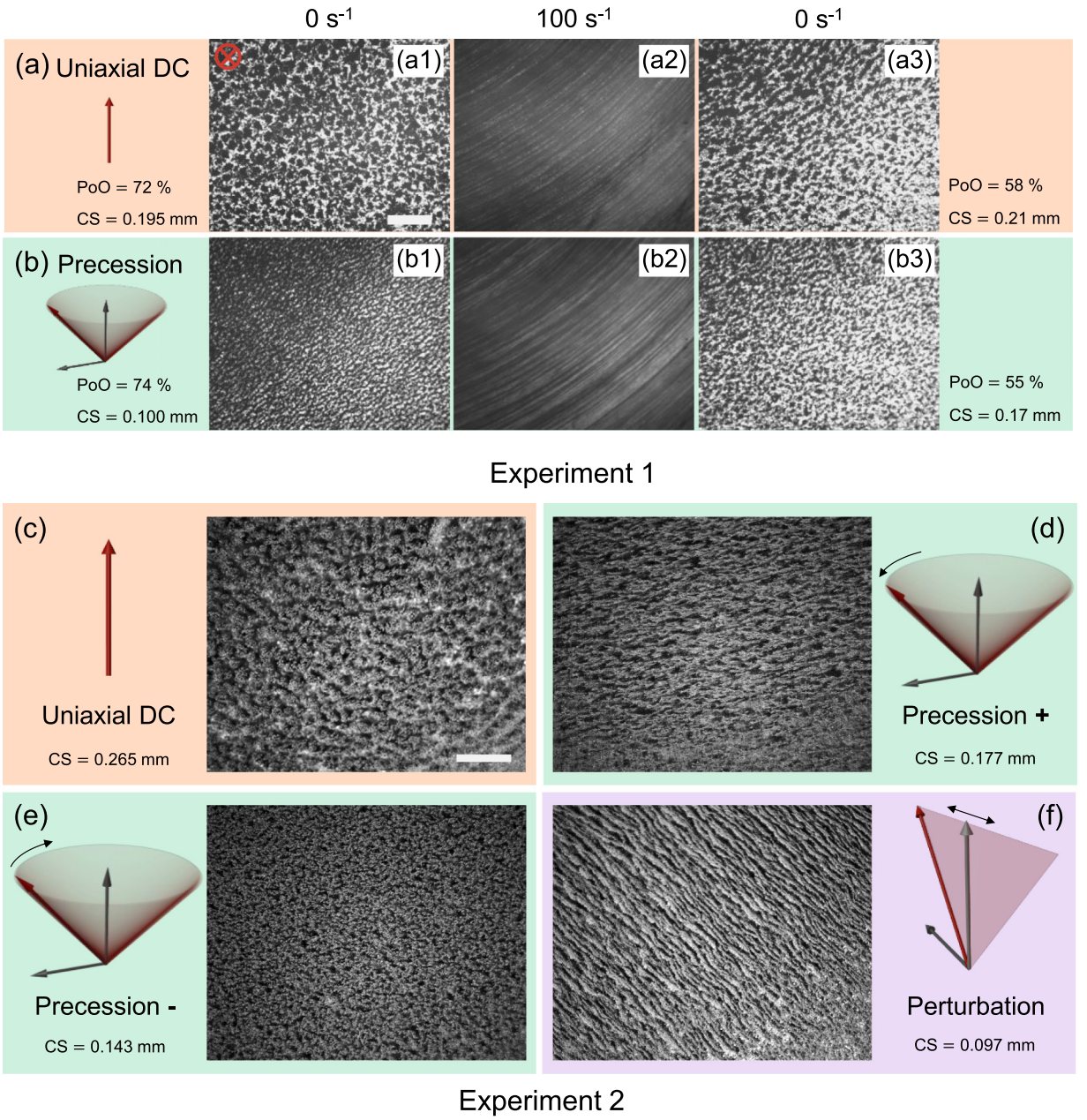

FIG. 4. Characteristic structures of a MR fluid under different combinations of shear flow and triaxial magnetic fields. Experiment 1: Snapshots of the generated structures under (a) uniaxial DC and (b) precession fields (angle of 25° and frequency of 1 Hz). (1) After self-assembly. (2) During shear rate sweep at $\dot{\gamma} = 100\,\mathrm{s}^{-1}$. (3) Once the shear rate sweep has finished. The percentage of occupation (PoO) and the characteristic size (CS) are calculated in (1) and (3). Note the preferred aggregate direction along the image diagonal in (b1) because that was the direction of the field xy component when the snapshot was taken. Experiment 2: Snapshots corresponding to the generated structures under different field configurations and a shear rate of $\dot{\gamma} = 3\,\mathrm{s}^{-1}$. Mean CS value at the end of the experiment is also included. PoO is 55% for all cases. (c) Uniaxial DC field. (d) Precession + field rotating in the same direction as the rheometer plate. (e) Same configuration as (d) but rotating in the opposite direction. (f) Perturbation field. Precession/Perturbation angle of 25° and frequency of 1 Hz. In both experiments, DC component of the fields is normal to the screen. Bar size: 500 μm.

yield stress) compared to those formed under precession fields.

The improved yield stress obtained under precession fields was explained in similar terms by Ref. [15], but in that case carrying out a structure analysis through particle-level simulations instead of experimental imaging. The only difference with that reference is the precession angle that maximizes the yield stress, 15° instead of 25° of the present work. This can be explained bearing in mind that here the particle concentration is smaller and thus, it requires a larger precession angle for the structures to sweep the surrounding volume and coalesce with neighbors.

The decreasing yield stress with increasing precession field frequency observed in Table II and Fig. 3(a) can be explained by considering that a higher frequency (and the corresponding increase in magnetic-field-induced Mn) causes particle

interactions to become time averaged. This impacts both the particle structures and their interactions. At low frequencies, the self-assembly mechanism involves dynamic sweeping and colliding, as previously described. However, at higher frequencies, the interactions are averaged over time, leading to static aggregates. This shift is evident when comparing the structural motion at 10 Hz and 100 Hz in Movie S2 (see the Supplemental Material [23]). As a result, the aggregates formed at higher frequencies are again open and defective, thus leading to lower yield stress. The image analysis did not reveal significant structural differences between the 1 Hz precession field and these higher frequencies. Moreover, the time-averaged interactions from the rotating component of the precession field counteract those from the DC component. As the frequency increases, the precession field effectively behaves like a uniaxial DC field of reduced magnitude. This weakened field may further compromise the quality of the aggregates formed during the assembly phase, contributing to the additional reduction in yield stress.

The previous discussion focuses on the yield stress of MR fluids at low flow-field-induced Mn. Once this threshold is exceeded, the sample exhibits flow behavior characterized by shear thinning, regardless of the field configuration used during self-assembly. This behavior is more clearly illustrated in the inset of Fig. 3(a), which shows the dimensionless viscosity η/η_∞ as a function of the flow-field-induced Mn. This representation, commonly used in the literature [8,24,25], highlights the similarities between the uniaxial DC field and the 1 Hz precession field in the postyield regime. Results for other precession frequencies follow a similar trend in this regime and are therefore not discussed further.

From a macroscopic point of view, the shear-thinning behavior is properly captured by the Casson model [22,25]. In terms of the flow-field-induced Mn, it reads as

$$\frac{\eta}{\eta_\infty} = 1 + \frac{\mathrm{Mn}^*}{\mathrm{Mn}} + 2\sqrt{\frac{\mathrm{Mn}^*}{\mathrm{Mn}}}, \tag{1}$$

where Mn^* is a volume fraction-dependent parameter known as critical Mason number. Basically, Mn^* is the ratio between the viscosity of the MR fluid at large shear rates, $\eta_\infty(\phi)$, and its yield stress, $\tau_y(\phi)$ [24]. Thus, Mn^* acts as a frontier between the magnetic- and hydrodynamic-controlled rheological regimes. Note that knowing the value of Mn^* for a MR fluid, its viscosity for any uniaxial DC field (along the flow gradient direction), or shear rate magnitude can be predicted with Eq. (1). Identifying $\eta_\infty(\phi)$ with the viscosity in the absence of magnetic fields [see linear fit—dashed line—in Fig. 3(a)], and taking $\tau_y(\phi)$ from finite element simulations [26] at 2.5 vol%, the resulting critical Mason number is $\mathrm{Mn}^* = 0.245$. This value was used to plot the Casson prediction in the inset of Fig. 3(a) (blue line) obtaining a reasonable agreement with the experimental flow curves measured with our proposed device.

All sets of experimental data collapse with each other and with the theoretical prediction at intermediate and high flow-field-induced Mn suggesting that the breaking process is similar no matter the field configuration used during the self-assembly. A movie of the microstructural evolution during the rheogram is shown in the Supplemental Material [23] (Movie S3). As can be seen, the initial structures break and give rise to a cylindrical layered pattern. This appears around $\dot{\gamma} = 100\,\mathrm{s}^{-1}$ or, in terms of the flow-field-induced Mn, $\mathrm{Mn} \sim 1$ in agreement with previous experiments reported in the literature [27]. Figures 4(a2) and 4(b2) are snapshots exactly at the layer onset, revealing the same microstructure in both experiments [indeed, data series in Fig. 3(a) intersect at $100\,\mathrm{s}^{-1}$]. The mean wavelength of the layers is similar in uniaxial DC and any precession field cases, $d \sim 0.18\,\mathrm{mm}$. This is not surprising because, upon the structure breakage, the layer formation is driven by the competition of the uniaxial DC field magnetostatics and the hydrodynamics induced by the flow. In the same sense, Figs. 4(a3) and 4(b3) show very similar structures in both cases once the rheogram has finished (rest state). The slightly higher PoO and CS values measured under uniaxial DC field (see darker top left corner of the corresponding Movie S3) can be attributed to particles that settled during the self-assembly step but were not incorporated into the chains. This occurs due to the static nature of the aggregation mechanism characteristic of DC fields, which limits the chain formation process and leaves some particles uncollected.

As demonstrated in Fig. 3(a), differences between the applied field configurations become more evident at small shear rates. In order to get a deeper insight on the yielding process at the early stage of the rheogram (small flow-field-induced Mn), we carried out a second kind of experiment where the field is suddenly applied under a constant shear rate of $3\,\mathrm{s}^{-1}$.

The resulting normalized stress $[\tau_N = [\tau(H) - \tau(H=0)]/\tau(H=0)]$ is shown in Fig. 3(b) for the different field configurations and frequencies. It can be seen that, despite the fact that the strength of the magnetic field (maximum strength for the perturbation one) is the same for the different tested configurations, the stress clearly changes. In particular, except for rotating fields, the unsteady fields give rise to larger stresses than the uniaxial DC field. As in the first experiment, the larger stress for unsteady fields is supported by a smaller CS meaning that unsteady fields induce structures that are more compact and resistant to be strained.

The time evolution of the microstructure and its corresponding CS values under different field configurations is presented in Movie S4 and Fig. S1 of the Supplemental Material [23]. For unsteady fields, only the 1 Hz case is shown. As anticipated based on the first experiment, uniaxial DC fields produce more open aggregates (larger CS) compared to other field configurations. Notably, the CS for the DC field is the only one that decreases over time, indicating that these loose structures gradually compact as shear is applied. Final (steady-state) CS values and structural snapshots are shown in Figs. 4(c)–4(f), which confirm the same correlation observed in the first experiment: larger CS values correspond to lower shear stress. Additionally, the snapshots distinguish between precession fields rotating in the same direction as the shear flow (PRE+) and those rotating in the opposite direction (PRE−). Despite this distinction, both configurations exhibit similar rheological behavior, which is why no distinction was made in Fig. 3(b).

For the rotating fields, it is noteworthy that their rheological response is significantly weaker [see the broken axis in Fig. 3(b)]. In this scenario, the field induces particle layers within the plane normal to the flow gradient direction. These layers experience minimal strain, meaning the stress response primarily arises from the viscous dissipation of the carrier fluid, which is sheared between the particle layers and the rheometer surfaces. Moreover, considering that these layers rotate in line with the field, the local shear rate experienced by the carrier fluid depends on the relative rotation direction. Specifically, under fields rotating opposite to the rheometer plate (ROT−), the fluid is subjected to a higher local shear rate compared to fields rotating in the same direction (ROT+). As expected, this results in higher shear stress for the ROT− configuration, as shown in Fig. 3(b). Since the rotating field plane is perpendicular to the optical axis, the induced layers block light transmission, preventing both imaging and further structural analysis.

Finally, we address the slight dependence of shear stress on the frequency of unsteady fields. By comparing the different columns for the same field configuration in Fig. 3(b), a slight decrease in shear stress is observed for precession fields, while an increase is seen for perturbation/rotating fields. However, no significant differences were found in terms of image analysis.

These opposite trends with frequency can be explained by the different aggregation mechanisms occurring at low and high magnetic-field-induced Mn. As described in the first experiment, precession fields at low frequencies promote the development of packed aggregates, as these can merge with neighboring aggregates through collisions while following the field's time evolution. However, as the frequency increases, the aggregates become static and experience a time-averaged interaction. For precession fields, this results in a classical interaction akin to that of a weaker uniaxial DC field. Consequently, as the frequency increases, the aggregates become more open, and the interaction between the particles weakens. Both factors contribute to a reduction in shear stress, as shown in Fig. 3(b).

In the case of perturbation and rotating fields, aggregation at low frequencies also occurs through collisions between chains, similar to the precession field mechanism. At higher frequencies, time-averaged interactions also emerge, but unlike precession fields, these interactions do not weaken the net particle interaction. Instead, for perturbation and rotating fields, the time-averaged interaction becomes attractive within the plane swept by the field. As a result, the aggregation mechanism shifts from being based on collisions (low magnetic-field-induced Mn) to one driven by attractive forces that hold the particles together in the field plane (high magnetic-field-induced Mn). Under strain, as the particles are pulled further apart, the attractive force resists this separation, leading to a higher shear stress signal.

III. CONCLUSIONS

Equipment has been developed to simultaneously investigate the mechanical properties and morphology of particle aggregates formed in magnetic suspensions under different magnetic field configurations. This equipment consists of a triaxial magnetic field generator comprising three pairs of identical orthogonal coils along the Cartesian axes. The generator is coupled with a rheometer in plate-plate configuration and allows high-speed imaging of the sample. The entire setup is synchronized with the rheometer's internal clock. Specifically, it has been found that the application of a precession field during the self-assembly phase induces a higher yield stress compared to uniaxial DC fields. This is reflected in the resulting columnar structures, which are more compact, interconnecting shear planes and offering greater resistance to the applied deformation compared to columns generated with the uniaxial DC field. Furthermore, it has been verified that different triaxial magnetic fields—uniaxial DC, precession, perturbation, and rotation—produce distinct levels of stress during shear deformation, which can be explained by the observed microstructure as certain types of structures exhibit higher flow resistance. The developed equipment opens up a wide range of possibilities in the experimental study of magnetic suspensions.

ACKNOWLEDGMENTS

This work was supported by Projects No. PID2022-138990NB-I00 and No. TED2021.129384B.C22 funded by MCIN/AEI/10.13039/501100011033 and by EU NextGenerationEU/ PRTR. O.M.C. acknowledges the financial support by PTA2023-023674-I. J.R.M. acknowledges the financial support by the (EFST)-H2020-MSCA-IF-2020 (Grant No. 101030666) fellowship. J.R.N. acknowledges the financial support by Investigo Program. G.C. acknowledges the financial support by the FPU20/04357 fellowship. A.R.B. acknowledges the financial support by the Juan de la Cierva FJC2021-047021-I.

APPENDIX: EXPERIMENTAL AND TECHNICAL DETAILS

1. Triaxial field generator

The RLC circuit of each axis is fed by a KEPCO BOP 20–10ML amplifier. Its inductive elements are the two coils connected in series (total inductance of 14.24 mH) while its capacitive element consists in a fractal bank of 12 capacitors offering more than 4000 different equivalent capacitances homogeneously distributed in the range [0.036, 310] μF. Total resistance of each circuit (5.7 Ω) comes from the coil resistivity plus a resistance of 1 Ω used to read actual values of the current through the circuit.

Type of current (steady or not), magnitude, phase, and frequency for each axis are imposed by the user through a GUI. This includes an automatic control system, running continuously, that sets the capacitor banks in the configurations with the closest resonance frequencies to the input ones, synchronizes the currents in the three axes, and also tunes the amplifier outputs till the actual currents meet the desired ones [28].

The interface and control system were developed in LabVIEW with a NI-DAQ controller and a PCIe-6343 card to stablish communications between the amplifiers, capacitor banks, and a computer (Intel Core i7-7700 @ 3.60GHz). Direct magnetic field measurements were made with a F.W.

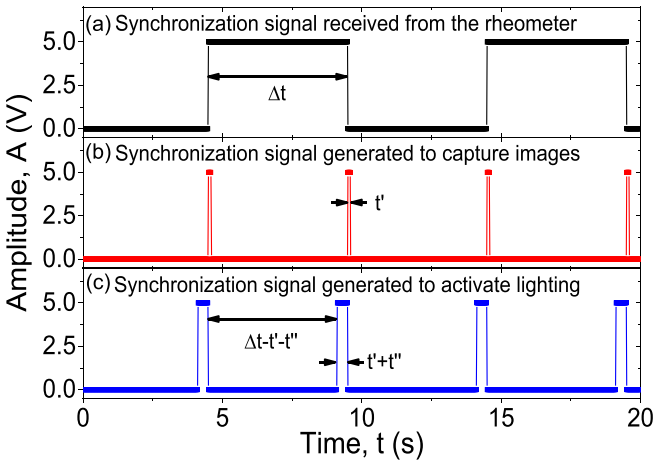

FIG. 5. Synchronization signals. Every logical change in the rheometer synchronization signals [(a), $\Delta t = 5$ s] generates a pulse of duration $t' = 100$ ms to capture images (b), when this pulse ends the lighting is deactivated and it is activated $t'' = 400$ ms before the next logical change in the rheometer synchronization signals arrives (c), so the light is turned on only 500 ms in each measurement point.

Bell 5170 teslameter equipped with a STH17-0404 transverse probe.

2. Synchronization

The long distance between the sample and the lens requires a highly intense and homogeneous light source. An LED ring (DF198-050, Advanced Illumination) positioned 1 cm below the sample is used for this purpose. In this configuration, the manufacturer's specifications indicate that the irradiance and luminance are approximately 703 klux and $223\mathrm{W/m^2}$, respectively. To prevent sample overheating, the light only turns on when capturing an image (flash mode). A hardware interface based on an Atmel microcontroller was developed to synchronize the rheometer, the high-speed camera, and the LED ring.

The interface accomplishes two main tasks. First, it corrects in real-time the synchronization signal generated by the rheometer to make it compatible with the camera and avoid losing images. Second, it generates the signal that switches the light on and off. The correction of the signal is necessary because the rheometer outputs rising and falling edges alternatively every time it takes a measurement [see Fig. 5(a), acquisition time of Δt], but the camera only captures images when it receives a rising edge, which results in capturing only half of the images.

Consequently, the microcontroller has been programmed with an interrupt routine that activates upon detecting a change in the logical level from the rheometer. Subsequently, it initiates a counter and produces a pulse (duration of t'), triggering the image capture process [Fig. 5(b)]. When this pulse ends, the LED is disabled, and it is activated t'' before the next change in the logical level occurs. This way, the light is only turned on for $t' + t''$ in each measurement interval of the rheometer [Fig. 5(c)]. The duration of the intervals (camera trigger t' and light activation $t' + t''$) can be manually adjusted, allowing it to be configured for different rheometer acquisition times Δt. Specific values used in this work can be found in the caption of Fig. 5.

3. Image analysis

In a first step, images are converted to black and white ones (using the Otsu's method) where aggregates are easily identified as groups of black pixels. To characterize them two metrics were studied. The first one is the percentage of occupation computed as the ratio of black pixels over the total number of pixels in the image. The second metric is the characteristic size of the system. It is calculated as the average wavelength of all pixel rows and columns of the image. The wavelength of each pixel line is calculated with the FFT.

4. MR fluid formulation

2.5 vol% concentration was chosen as a compromise between getting a measurable rheological response and imaging distinguishable (noncrowded) particle structures. As carrier liquid we used glycerol (Scharlau, 86–88%) mixed with distilled water at a concentration 75:25, so that its final viscosity was ~ 10 mPa·s. The particulate phase was carbonyl iron microparticles (EW grade, BASF). Those have a contrast factor of $\beta = 0.64$ for an external field strength of $H = 4\ \mathrm{kA \cdot m^{-1}}$.

5. Rheological experiments

A torsional rheometer (MCR501 Anton Paar) with a plate-plate configuration was used. Plate diameter and gap between plates were 20 mm and 300 μm, respectively. With this geometry, the minimum measurable shear stress was 0.05 Pa. All experiments were repeated three times using fresh new samples and include a preshear step before the measurement to homogenize the sample and remove its mechanical history. Regarding the duration of the self-assembly step in the first experiment (30 s), longer steps (60 and 90 s) were also tested yielding similar results (differences below 4%).

[1] *Magnetorheology Advances and Applications*, edited by N. M. Wereley (Royal Society of Chemistry, London, 2013).
[2] *Magnetorheological Materials and Their Applications*, edited by S. B. Choi and W. Li (Institution of Engineering and Technology, Stevenage, 2019).
[3] J. R. Morillas and J. de Vicente, Magnetorheology: A review, Soft Matter **16**, 9614 (2020).
[4] *Magnetic Soft Matter: Fundamentals and Applications*, edited by J. de Vicente (Royal Society of Chemistry, London, 2023).
[5] M. Hagenbüchle and J. Liu, Chain formation and chain dynamics in a dilute magnetorheological fluid, Appl. Optics **36**, 7664 (1997).
[6] G. Bossis, S. Lacis, A. Meunier, and O. Volkova, Magnetorheological fluids, J. Magn. Magn. Mater **252**, 224 (2002).

[7] K. Shahrivar, E. Carreón-González, J. R. Morillas, and J. de Vicente, Aggregation kinetics of carbonyl iron based magnetic suspensions in 2D, Soft Matter **13**, 2677 (2017).

[8] J. R. Morillas and J. de Vicente, Physics of Magnetorheological Fluids, *Encyclopedia of Smart Materials*, (Elsevier, Amsterdam, 2022), Vol. 5.

[9] O. Volkova, G. Bossis, M. Guyot, V. Bashtovoi, and A. Reks, Magnetorheology of magnetic holes compared to magnetic particles, J. Rheol. **44**, 91 (2000).

[10] S. Melle, O. G. Calderón, G. G. Fuller, and M. A. Rubio, Polarizable particle aggregation under rotating magnetic fields using scattering dichroism, J. Colloid Interface Sci **247**, 200 (2002).

[11] F. Donado, U. Sandoval, and J. L. Carrillo, Kinetics of aggregation in non-Brownian magnetic particle dispersions in the presence of perturbations, Phys. Rev. E **79**, 011406 (2009).

[12] J. E. Martin and A. Snezhko, Driving self-assembly and emergent dynamics in colloidal suspensions by time-dependent magnetic fields, Rep. Prog. Phys **76**, 126601 (2013).

[13] M. Terkel and J. de Vicente, Magnetorheology of exotic magnetic mesostructures generated under triaxial unsteady magnetic fields, Smart Mater. Struct **30**, 014005 (2020).

[14] A. Spatafora-Salazar, D. M. Lobmeyer, L. H. P. Cunha, K. Joshi, and S. L. Biswal, Hierarchical assemblies of superparamagnetic colloids in time-varying magnetic fields, Soft Matter **17**, 1120 (2021).

[15] M. Terkel, J. Tajuelo, and J. de Vicente, Enhancing magnetorheology with precession magnetic fields, J. Rheol **66**, 67 (2022).

[16] M. Terkel, R. Wright, and J. de Vicente, Magnetorheology in unsteady fields: From uniaxial DC to rotating AC fields, J. Rheol **67**, 833 (2023).

[17] J. E. Martin, R. A. Anderson, and R. L. Williamson, Generating strange magnetic and dielectric interactions: Classical molecules and particle foams, J. Chem. Phys **118**, 1557 (2003).

[18] J. E. Martin, Theory of strong intrinsic mixing of particle suspensions in vortex magnetic fields, Phys. Rev. E **79**, 011503 (2009).

[19] J. E. Martin, A resonant biaxial Helmholtz coil employing a fractal capacitor bank, Rev. Sci. Instrum **84**, 094704 (2013).

[20] L. Rossi, D. Doorly, and D. Kustrin, Lamination and mixing in three fundamental flow sequences driven by electromagnetic body forces, Phys. Rev. E **86**, 026313 (2012).

[21] A. Figueroa, S. Cuevas, and E. Ramos, Lissajous trajectories in electromagnetically driven vortices, J. Fluid Mech **815**, 415 (2017).

[22] C. L. A. Berli and J. de Vicente, A structural viscosity model for magnetorheology, Appl. Phys Lett **101**, 021903 (2012).

[23] See Supplemental Material at http://link.aps.org/supplemental/10.1103/PhysRevE.111.025415 for the supplemental movies accompanying the experiments as well as the CS and PoO time evolutions during the second experiment.

[24] S. G. Sherman, A. C. Becnel, and N. M. Wereley, Relating Mason number to Bingham number in magnetorheological fluids, J. Magn. Magn. Mater **380**, 98 (2015).

[25] D. Susan-Resiga and L. Vékás, Ferrofluid based composite fluids: Magnetorheological properties correlated by Mason and Casson numbers, J. Rheol **61**, 401 (2017).

[26] J. R. Morillas and J. de Vicente, Yielding behavior of model magnetorheological fluids, Soft Matter **15**, 3330 (2019).

[27] O. Volkova, S. Cutillas, and G. Bossis, Shear banded flows and nematic-to-isotropic transition in ER and MR fluids, Phys. Rev. Lett **82**, 233 (1999).

[28] J. Tajuelo, Ó. Martínez-Cano, J. R. Morillas, J. Yang, and J. de Vicente, Generation of synchronized high-frequency triaxial magnetic fields using fractal capacitor banks, Phys. Rev. Appli. **20**, 044063 (2023).